The antiferromagnetic S = 1/2 Heisenberg model on the C60 fullerene geometry

Rausch, R.; Plorin, C.; Peschke, M.

The antiferromagnetic $S = 1/2$ Heisenberg model on the C_{60} fullerene geometry

Roman Rausch[1,2⋆], **Cassian Plorin**[3] **and Matthias Peschke**[4]

1 Technische Universität Braunschweig, Institut für Mathematische Physik,
Mendelssohnstraße 3, 38106 Braunschweig, Germany
2 Department of Physics, Kyoto University, Kyoto 606-8502, Japan
3 Department of Physics, University of Hamburg,
Jungiusstraße 9, D-20355 Hamburg, Germany
4 Institute for Theoretical Physics Amsterdam and Delta Institute for Theoretical Physics,
University of Amsterdam, Science Park 904, 1098 XH Amsterdam, The Netherlands

⋆ r.rausch@tu-braunschweig.de

Abstract

We solve the quantum-mechanical antiferromagnetic Heisenberg model with spins positioned on vertices of the truncated icosahedron using the density-matrix renormalization group (DMRG). This describes magnetic properties of the undoped C_{60} fullerene at half filling in the limit of strong on-site interaction U. We calculate the ground state and correlation functions for all possible distances, the lowest singlet and triplet excited states, as well as thermodynamic properties, namely the specific heat and spin susceptibility. We find that unlike smaller C_{20} or C_{32} that are solvable by exact diagonalization, the lowest excited state is a triplet rather than a singlet, indicating a reduced frustration due to the presence of many hexagon faces and the separation of the pentagonal faces, similar to what is found for the truncated tetrahedron. This implies that frustration may be tuneable within the fullerenes by changing their size. The spin-spin correlations are much stronger along the hexagon bonds and exponentially decrease with distance, so that the molecule is large enough not to be correlated across its whole extent. The specific heat shows a high-temperature peak and a low-temperature shoulder reminiscent of the kagomé lattice, while the spin susceptibility shows a single broad peak and is very close to the one of C_{20}.

Contents

1   Introduction

The C_{60} buckminsterfullerene molecule, where 60 carbon atoms sit on the vertices of a truncated icosahedron, is a prominent molecule with a wealth of chemical and nanotechnological applications [1–3], and is also of interest in terms of correlated-electron physics. A lattice of C_{60} molecules becomes superconducting when doped with alkali metals [4–7], with a critical temperature of around 40K. This is unusually high for a typical phononic mechanism, so that an electronic mechanism that results from an on-site Hubbard interaction U is under discussion as well [8, 9]. At half filling (no doping), a strong U is well-known to cause electron localization via the Mott mechanism and the resulting low-energy properties are described by the antiferromagnetic spin-1/2 Heisenberg model

$$H = J \sum_{\langle ij \rangle} \mathbf{S}_i \cdot \mathbf{S}_j, \tag{1}$$

where $\mathbf{S}_i$ is the spin operator at site i, $J = 4t^2/U > 0$ is the exchange integral and t is the hopping integral between nearest-neighbour sites i and j.

However, the prototypical Mott systems are transition metal oxides with strong Coulomb repulsion in a narrow d-band, while in carbon atoms, we are dealing with a valence p-band. As a consequence, while the nearest-neighbour hopping parameters are estimated around $2-3$ eV, the Hubbard repulsion U is estimated to be around 9 eV [10–12], which would place the system into the intermediate-coupling range. Still, since solving the full Hubbard model for 60 orbitals on a 2D-like geometry is a hard problem, we may attempt to understand the Heisenberg approximation first. Other authors have argued that there should only be a quantitative difference [12], since the system is finite. The Hartree-Fock solution shows a phase transition to magnetic order at $U_c/t \approx 2.6$ [13]. This seems to indicate that local moments may be already well-formed for a fairly small U. As soon as they are formed, mean field is biased towards an ordered solution, but we expect the exact ground state of this finite system to always be a singlet.

Apart from trying to approximate the Hubbard model, a spin model on a fullerene-type geometry is interesting on its own, being connected to the problem of frustrated spin systems. These arise on non-bipartite geometries like the triangular, kagomé or pyrochlore lattice, with building blocks of three-site clusters that cannot accommodate antiferromagnetic bonds in a commensurate fashion. This tends to induce spin-liquid states that are disordered and non-trivial [14–21]. In fullerenes, we instead find 12 pentagon clusters that are also frustrated due

to the odd amount of sites. This has no strict correspondence in the 2D plane, since a tiling by regular pentagons is not possible. However, a Cairo tiling is possible by irregular pentagons, resulting in two bonds J and J' [22]. While non-bipartite, this lattice can be divided into two inequivalent sublattices, tends to show ferrimagnetic order, and is thus quite different from our case [22].

A frustrated spin system is still quite challenging for a theoretical description. For example, the infamous sign problem [23] inhibits an efficient simulation with the Quantum Monte Carlo technique. However, tensor-network approaches do not suffer from it. C_{60} is in particular well-suited to a solution using the density-matrix renormalization group (DMRG) [24] due to its finite and very manageable amount of sites.

The truncated icosahedron is part of the icosahedral group I_h. To its members belong two of the Platonic solids, the icosahedron with 12 sites and the dodecahedron with 20 sites (which is also the smallest fullerene C_{20}) [25]. The former has only triangular plaquettes, the latter only pentagonal ones, and both are small enough to be solved by full diagonalization if spatial symmetries are exploited to reduce the Hilbert space size [26]. I_h also has 5 members within the Archimedean solids, of which the icosidodecahedron with 30 sites (triangular and pentagonal faces) has been the subject of particularly intense study [27–31], since this is the geometry of the magnetic atoms in the Keplerate molecules $\{Mo_{72}V_{30}\}$, $\{Mo_{72}Cr_{30}\}$ and $\{Mo_{72}Fe_{30}\}$, with $S = 1/2, 3/2$ and $5/2$ respectively [32–34]. It is solvable by exact diagonalization for $S = 1/2$ [27]. Small fullerenes up to C_{32} can also be solved by exact diagonalization [35,36], but have different symmetries. Finally, the truncated tetrahedron is a 12-vertex Archimedean solid, which is not a member of I_h, but has a geometry that is similar to C_{60} [13,37,38], consisting out of four triangles separated by hexagons. For this reason, it is often also counted as a fullerene C_{12}. All these smaller molecules offer a very useful comparison and benchmark.

Each fullerene C_n contains $n/2 - 10$ hexagons and 12 pentagons [39], so that for $n \geq 44$ the number of hexagon faces starts to dominate. For $n \to \infty$, we can expect that the fullerene properties approach those of a hexagonal lattice. But without undertaking the full calculation, it is impossible to say where exactly the crossover happens or what properties might be retained in the large-n limit. In fact, the small fullerenes up to C_{32} do not behave monotonously [35]: For example, the ground-state energy for C_{26} and C_{28} is larger than for C_{20} and the first excited state for C_{28} is a triplet instead of a singlet.

In this paper, we present the solution of the Heisenberg model on the C_{60} geometry. Previous works treated the problem classically [12] or approximately [23], while our calculation is very precise for the ground state. Jiang and Kivelson solved the $t-J$ model on C_{60} [8], which should coincide with our result at half filling. However, they discussed very different questions; and we further present results for the lowest excited states as well as thermodynamics.

Due to two dissimilar types of nearest-neighbour bonds, the corresponding hopping integrals may be slightly different, $t_1 \approx 1.2\, t_2$, leading to different exchange couplings $J_1 \neq J_2$ [12,40]. For simplicity, we ignore this fact and use a homogeneous $J = J_1 = J_2$ for all bonds. The correlations along the bonds turn out to be nonetheless very different as a consequence of the geometry, as will be seen below. We take $J = 1$ as the energy scale, giving all energies in units of J and all temperatures in units of J/k_B, where k_B is the Boltzmann constant.

2 Ground state and correlation functions

2.1 Technical notes

Our code incorporates the spin-SU(2) symmetry of the model following Ref. [41], which reduces both the bond dimension of the matrix-product state (MPS) representation of the wave-

function and the matrix-product operator (MPO) representation of the Hamiltonian. The latter can be further reduced using the lossless compression algorithm of Ref. [42]. It gives only a small benefit of 8% reduction for H itself, with the resulting maximal MPO bond dimension of $\chi(H) = 35 \times 32$ (from 38×35). The benefit for H^2 is larger, yielding $\chi(H^2) = 564 \times 468$ (reduced from 1444×1225, hence by 55%). With these optimizations, the ground state can be found quite efficiently and we can take the variance per site

$$\Delta E^2/L = \left(\langle H^2 \rangle - E^2\right)/L, \tag{2}$$

as a global error measure that is immune to local minima.

Since DMRG requires a linear chain of sites, we must map the C_{60} vertices onto it, which creates long-range spin-spin interactions across it. The important factors to consider are: 1. the maximal hopping range (the bandwidth of the corresponding graph), 2. the average hopping range, 3. the fact that DMRG is particularly good for nearest-neighbour bonds on the chain, so that a representation where the sites i and $i+1$ are connected should be beneficial (this will also be practical for finite-temperature calculations further below). Our mapping is an infalling spiral on the Schlegel diagram, such that the first and last site have maximal distance, and is shown in Fig. 4. We have also tried out the mapping of Jiang and Kivelson [8] and a graph compression using the Cuthill-McKee algorithm [43]; and find similar MPO compression and ground state convergence results. A random permutation of the sites, on the other hand, leads to a representation with a large MPO bond dimension which the compression algorithm is unable to decrease, and the convergence becomes much worse. For a benchmark with a system solvable by exact diagonalization, we compare a similar spiral mapping for the icosidodecahedron with the mapping used by Exler and Schnack [29,44] and find that both approaches come within 99.97% of the exact $S = 1/2$ ground-state energy [22] at a bond dimension of $\chi_{SU(2)} = 500$. Thus we conclude that as long as the numbering of the sites is reasonable and more or less minimizes the hopping distances, the dependence on the numbering itself is small and an inaccuracy that results from a suboptimal numbering can simply be compensated by moderately increasing the bond dimension. This is in line with the conclusions of Ummethum, Schnack and Läuchli [29]. Finally, we note that by checking the energy variance (Eq. 2) and the distribution of spin-spin correlations at a given distance (see Sec. 2.3), we have good independent error measures.

Interestingly, we find that the number of required subspaces per site in the DMRG simulation is similar to the Heisenberg chain (around seven), but each subspace requires large matrices (with $3500 \sim 4000$ rows/columns, see Tab. 1). This makes the simulation very memory-intensive, requiring several hundred GB of RAM for good precision.

2.2 Energy

The ground state lies in the singlet sector with $S_{\text{tot}} = \sum_i \langle \mathbf{S}_i \rangle = 0$ (see Tab. 1). The energy per spin is found to be $E_0/L = -0.51886$. This is lower than the previous result of $E_0/L = -0.50798$ obtained by a spin-wave calculation on top of the classical ground state [23].

Looking at the change in ground-state energy with molecule size, we may compare with the truncated tetrahedron C_{12} ($E_0/L = -0.475076$), C_{20} ($E_0/L = -0.486109$) and C_{32} ($E_0/L = -0.4980$ [35]), and recognize that the value indeed slowly approaches the one for the hexagonal lattice $E_0/L \approx -0.55$ [45]. On the other hand, it is quite close to the much smaller icosahedron ($E_0/L = -0.515657$) which has the same icosahedral symmetry, but only contains triangular plaquettes. Finally, the icosidodecahedron has the highest energy $E_0/L = -0.441141$ [22], probably due to the strong frustration.

Table 1: Properties of the ground state and the lowest eigenstates: total energy E, energy density E/L, the gap to the ground state, the total spin S_{tot}, the full bond dimension $\chi_{\text{SU(2)}}$ with spin-SU(2) symmetry, the maximal bond dimension of the largest subspace $\chi_{\text{sub,SU(2)}}$, the effective bond dimension χ_{eff} that would be required when not exploiting the symmetry, the energy variance per site (Eq. 2), and the overlap with the ground state.

E	E/L	gap	S_{tot}	$\chi_{\text{SU(2)}}$	$\chi_{\text{sub,SU(2)}}$	χ_{eff}	$\Delta E^2/L$	GS overlap
-31.131(7)	-0.51886(1)	-	0	10000	3966	43146	$8 \cdot 10^{-5}$	-
-30.775(6)	-0.51292(7)	0.356(0)	1	10000	3770	44302	$1.9 \cdot 10^{-4}$	0
-30.440(9)	-0.50734(9)	0.690(8)	0	10000	3582	46846	$1.6 \cdot 10^{-4}$	$\sim 10^{-8}$
-30.3(2)	-0.505(3)	0.8(2)	2	5000	1855	24546	$1.4 \cdot 10^{-3}$	0

2.3 Correlation functions

The truncated icosahedron is an Archimedean solid, so that all of its sites (vertices) are equivalent; but since two hexagons and one pentagon come together at a vertex, there are two different nearest-neighbour bonds: one that is shared between the two hexagons and two that run between a pentagon and a hexagon (with the total count of 30 and 60, respectively, see Fig. 3 and Fig. 4). We shall call them "hexagon bonds" (H-bonds) and "pentagon bonds" (P-bonds). The wavefunction must respect this geometry, but as the mapping to a chain introduces a bias, this only happens for a sufficiently large bond dimension. Thus, we can average over the respective bonds and take the resulting distribution width as a measure of error, with a δ-distribution expected in the limit of $\chi \to \infty$. Figure 1 shows the result for distances up to $d = 4$, from which we see that for the given bond dimension, the distributions have already become sufficiently sharp.

Similarly, we have up to five distinct types of bonds for the remaining distances $d = 2-9$. In the numerics, they can be distinguished as distinct peaks in the distribution of the correlations $\langle \mathbf{S} \cdot \mathbf{S}_d \rangle$ (Figs. 1 and 2). Up to $d = 4$ we classify them by a sequence of H- and P-bonds. For example, at $d = 2$ we have two PP-bonds by going along the P-bonds twice, ending up in the same-face pentagon of a given vertex; and four HP-bonds, by going along H and P (in any order), ending up in the same-face hexagon (see Fig. 3).

A striking pattern is that the path that can be labelled by alternating H- and P-bonds has the strongest correlations at each d. Such a path is possible up to $d = 7$; and up to $d = 3$, it ends in the same-face hexagon. Hence, it seems that since the hexagons are not frustrated, putting a lot of correlation into these bonds can lower the energy more effectively. In fact, the sequence of intrahexagon values is closely matched by the infinite Heisenberg chain [46] or the $L = 6$ Heisenberg ring. On the other hand, the bonds involving pentagons are closely matched by the values of the dodecahedron. Figure 5 shows a comparison. As a consequence of this, the ground-state energy can actually be naively approximated by taking $E_0 \approx 30 \langle \mathbf{S} \cdot \mathbf{S}_{d=1} \rangle [\text{chain}] + 60 \langle \mathbf{S} \cdot \mathbf{S}_{d=1} \rangle [\text{dodecahedron}] \approx -32.739$, coming within 95% of the precise DMRG value.

Finally, we also note that for $d = 5, 6, 7$ the correlations acquire mixed signs and for $d = 8, 9$ the staggered antiferromagnetic order is flipped, i.e. we have $\langle \mathbf{S} \cdot \mathbf{S}_{d=8} \rangle < 0$ and $\langle \mathbf{S} \cdot \mathbf{S}_{d=9} \rangle > 0$.

Overall, the pattern is very similar to the truncated tetrahedron, where the maximal distance is $d = 3$, the stronger correlations are also found for the same-face hexagon bonds; and a mixed sign is acquired for $d = 3$ (see Fig. 5).

Looking at the decay of the correlations with distance, we find $\xi \sim 1.4$ when an exponential fit $\left| \langle \mathbf{S} \cdot \mathbf{S}_d \rangle \right| \sim \exp(-d/\xi)$ is applied to the maximal absolute values and $\xi \sim 1.2$ if it is applied to bond-averaged values (see inset of Fig. 5) Previously, $\xi = 3 \sim 4$ was proposed [23] based

Table 2: Comparison of the singlet and triplet gaps for various polyhedra with L vertices. The smaller value is underlined.

polyhedron	L	singlet gap	triplet gap
trunc. tetrahedron (C_{12})	12	0.896	<u>0.688</u>
icosahedron	12	<u>0.533</u>	0.900
dodecahedron (C_{20})	20	<u>0.316</u>	0.514
icosidodecahedron	30	<u>0.047</u>	0.218
trunc. icosahedron (C_{60})	60	0.691	<u>0.356</u>

on a strong-coupling Quantum Monte Carlo study of the single-band Hubbard model. The truncated tetrahedron and the dodecahedron have larger excitation gaps, but the maximum possible distance is $d = 3$ and $d = 5$, respectively, so that they are correlated over practically their whole extent (see Fig. 5). The icosidodecahedron has a small gap, but the behaviour of the correlations is very similar to the dodecahedron. An exponential fit does not give good results for these small molecules. For C_{60}, the smallest gap is actually about as large as for the dodecahedron, but the maximal distance is $d = 9$ and the drop-off across the whole molecule is larger. In this sense, the C_{60} spin state is disordered.

The fullerenes C_n have a kind of thermodynamic limit $n \to \infty$, where we expect that the magnetic properties should approach the properties of the hexagonal lattice with Néel order [47], which should be detectable by large spin-spin correlations in a finite system. Clearly, we are still far away from that limit: The pentagons disrupt the bipartiteness and lead to a disordered state instead.

3 Lowest triplet and singlet excitations

By fixing $S_{\text{tot}} = 1$, we can compute the lowest excited state in the triplet sector and look at its properties as well. We limit ourselves to the expectation value of the local spin $\langle \mathbf{S}_i \rangle$ and the nearest-neighbour correlation functions. The values of $\langle \mathbf{S}_i \rangle$ are shown in Fig. 6. We observe that a good part of the angular momentum (about 60%) localizes on a 20-site ring along a "meridian" of the molecule. As this breaks the spatial symmetry, we conclude that the lowest $S_{\text{tot}} = 1$ state is degenerate beyond the three components of the spin projection, i.e. has a multiplicity > 1 of its irreducible point group representation. The symmetry should be restored when averaging over the whole degenerate subspace.

The icosahedral group has the irreducible representations A (1), T (3), F (4) and H (5) [48], where the brackets indicate the multiplicity. The members of the icosahedral group that are solvable by exact diagonalization behave as follows: The lowest triplets of the icosahedron transform as T_{2g}, T_{1u} and T_{2u}; of the dodecahedron as T_{2g}, F_u, T_{2u} [26]; and of the icosidodecahedron as A_g, H_u, H_g [22]. Hence, while the lowest triplet is 3-fold degenerate for the former two, it is nondegenerate for the latter. Our results indicate that the lowest triplet of C_{60} is again degenerate.

Finding out its irreducible representation requires either to work within a symmetry-adapted basis or to construct the whole multiplet of excited states. Since the degeneracy is at least 3-fold, we would need at least the lowest four eigenstates in the $S = 1$ sector to a precision that is smaller than the gap to the next triplet state. Since the degeneracy of the excited states is of no crucial physical importance, we do not attempt this procedure in our work.
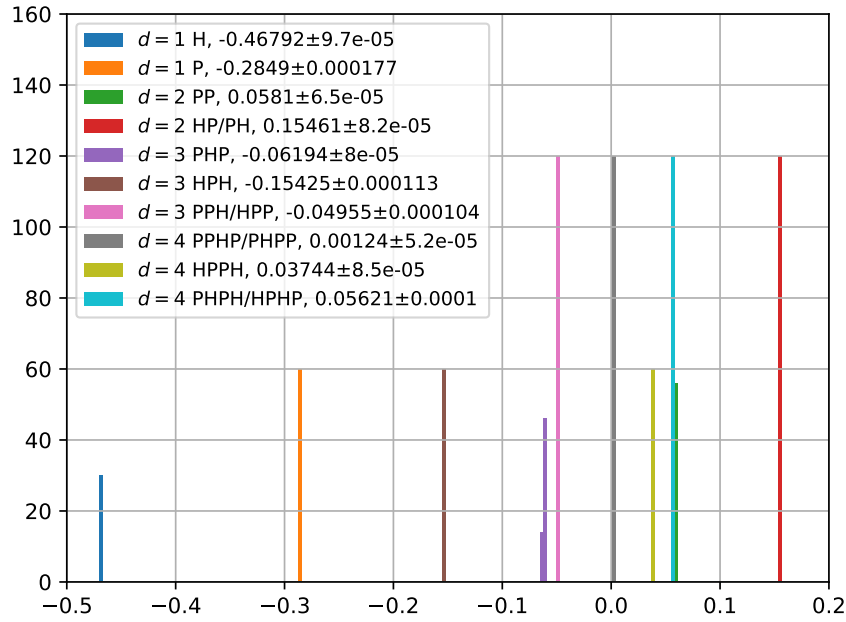
Figure 1: Histogram of the spin-spin correlation function $\langle \mathbf{S} \cdot \mathbf{S}_d \rangle$ in the ground state for distances $d = 1$ to 4 and the various types of C_{60} bonds. For the meaning of the labels, see Fig. 3 and the explanation in the text. The standard deviation of the distribution is taken as the error measure in the legend. The binsize is 0.003.
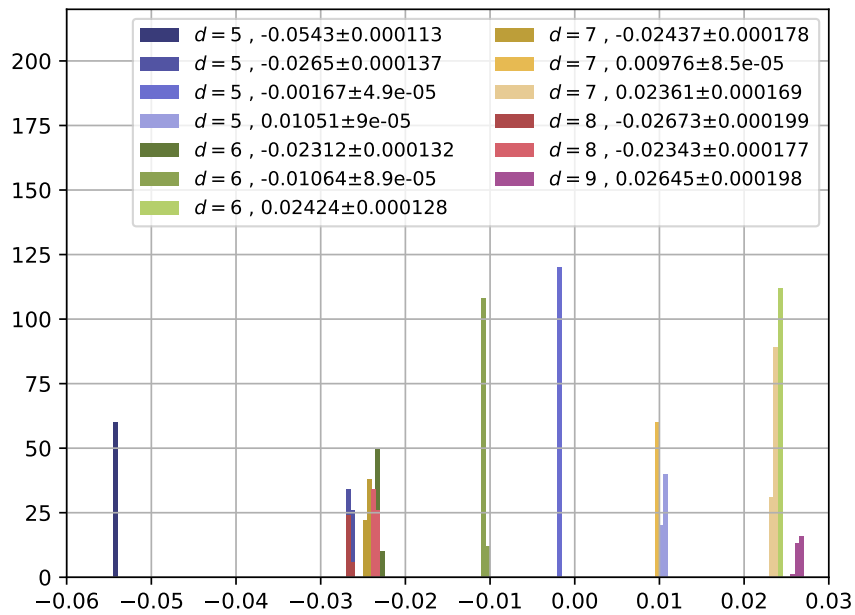

Figure 2: Histogram of the spin-spin correlation function $\langle \mathbf{S} \cdot \mathbf{S}_d \rangle$ in the ground state for distances $d = 5$ to 9 and the various types of C_{60} bonds. The standard deviation of the distribution is taken as the error measure in the legend. The binsize is 0.0005.
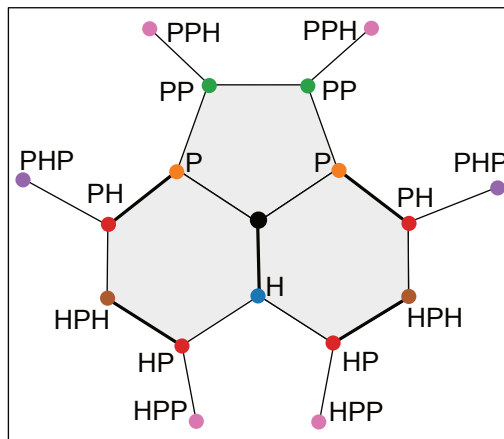
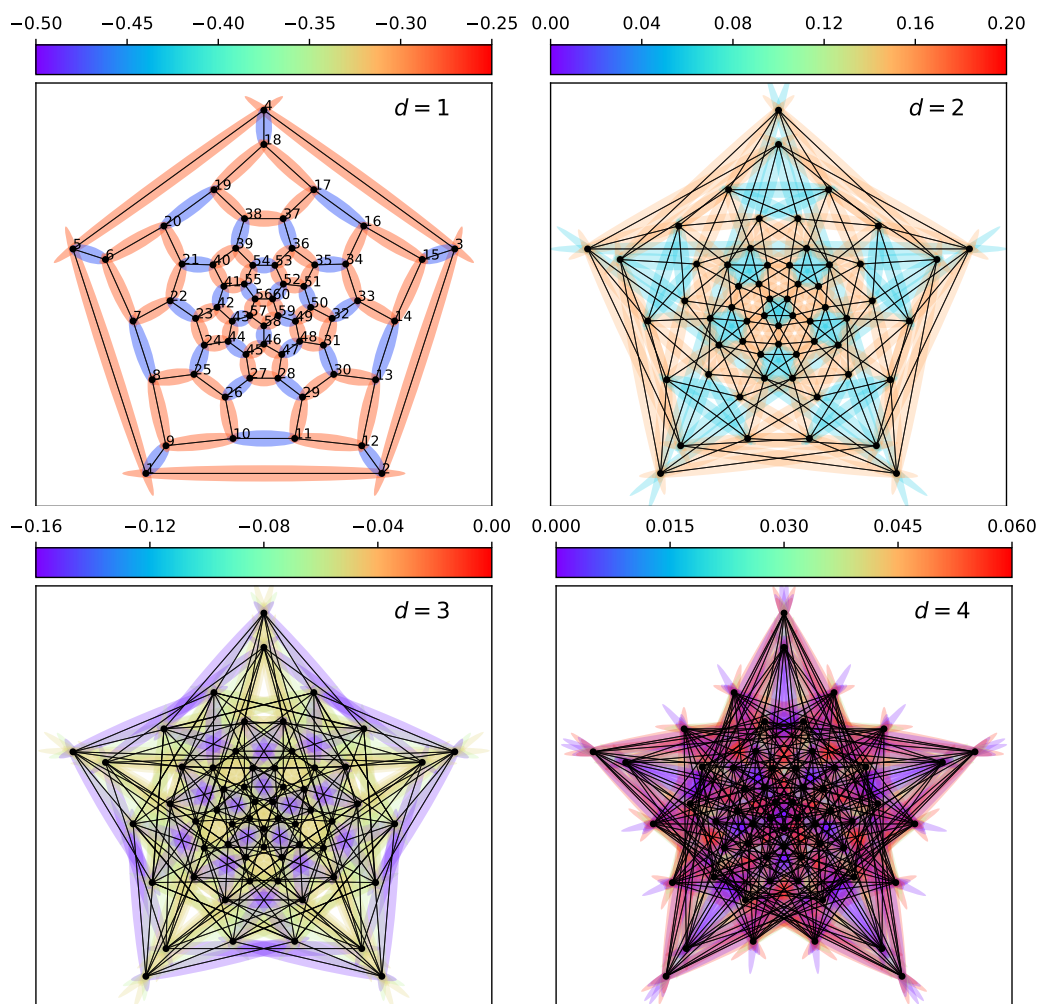Figure 3: Neighbourhood of a given site (black circle) showing the various types of bonds (cf. Fig. 1).

Figure 4: Visualization of the spin-spin correlation function $\langle \mathbf{S} \cdot \mathbf{S}_d \rangle$ in the ground state for distances $d = 1, 2, 3, 4$ in real space on the planar Schlegel projection of C_{60}. The plot for $d = 1$ also shows the chosen enumeration of the sites.

We find that the symmetry-breaking 20-site ring is remarkably robust in our DMRG simulation and arises from different random starting states and for different site enumerations. In a
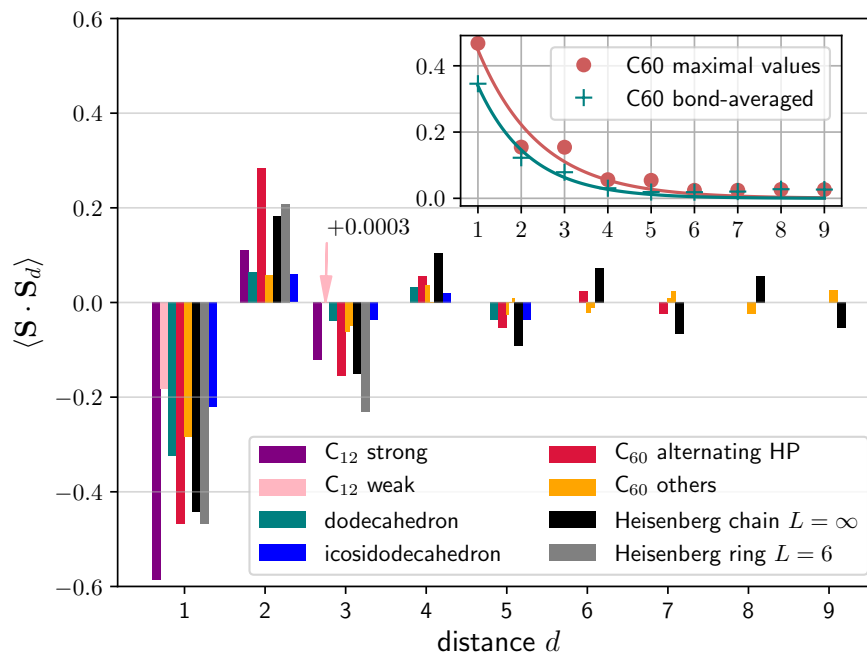
Figure 5: Comparison of the spin-spin correlation function between different geometries: analytical values for the infinite Heisenberg chain [46], numerically exact values for the $L = 6$ Heisenberg ring, C_{12} (truncated tetrahedron) and the dodecahedron [26]. The icosidodecahedron values are according to our own DMRG calculation. The C_{60} alternating HP bonds are formed by alternating jumps along H and P (cf. Fig. 3), starting with H; and link two sites within a hexagon up to $d = 3$. Note that the icosidodecahedron has two inequivalent bonds for $d = 2, 3, 4$, but the correlation along the second-type bond is very small and is omitted. The weak bond for C_{12} at $d = 3$ is +0.0003 and thus barely visible. The inset shows an exponential fit for the distance dependence of the C_{60} spin-spin correlations, either by taking the maximal values for each d or by taking bond-averaged values.

realistic setting, we expect that the spatial symmetry would in any case be at least slightly broken by the Jahn-Teller effect, so that such a state may split from the degenerate subspace. In fact, for doped C_{60}, one observes the same preference for a localization of the excess electron along a 20-site ring [49], whereas in our case this happens to a doped spin (excess angular momentum).

A striking property of Heisenberg spins on smaller icosahedral molecules [22, 26], as well as for smaller fullerene geometries [35], is that the first excited state is not a triplet, but rather a singlet, a signature of frustration connected to spin-liquid behaviour [14, 50–52]. The icosidodecahedron has in fact a large amount of singlet states below the first triplet [22]. On the other hand, for the truncated tetrahedron, the first excited state is a triplet for $S = 1/2$.

We therefore calculate the first excited state in the singlet sector ($S_{\text{tot}} = 0$) as the lowest state of the Hamiltonian $\tilde{H} = H + E_p \lvert E_0 \rangle \langle E_0 \rvert$ with a sufficiently large energy penalty $E_p > 0$ that must be larger than the neutral gap. The result is shown in Tab. 1. The neutral gap $\Delta_{S=0} = E_1(S_{\text{tot}} = 0) - E_0(S_{\text{tot}=0}) = 0.691$ turns out to be significantly larger than the singlet-triplet gap $\Delta_{S=1} = E_0(S_{\text{tot}} = 1) - E_0(S_{\text{tot}=0}) = 0.356$ (cf. the other polyhedra in Tab. 2). We attribute this behaviour to the reduced frustration of the C_{60} molecule due to the large amount of hexagonal faces. Furthermore, we note that all the pentagonal faces are completely separated by the hexagons, so that regions with adjacent frustrated pentagons that are present in smaller fullerenes are broken up in C_{60}.
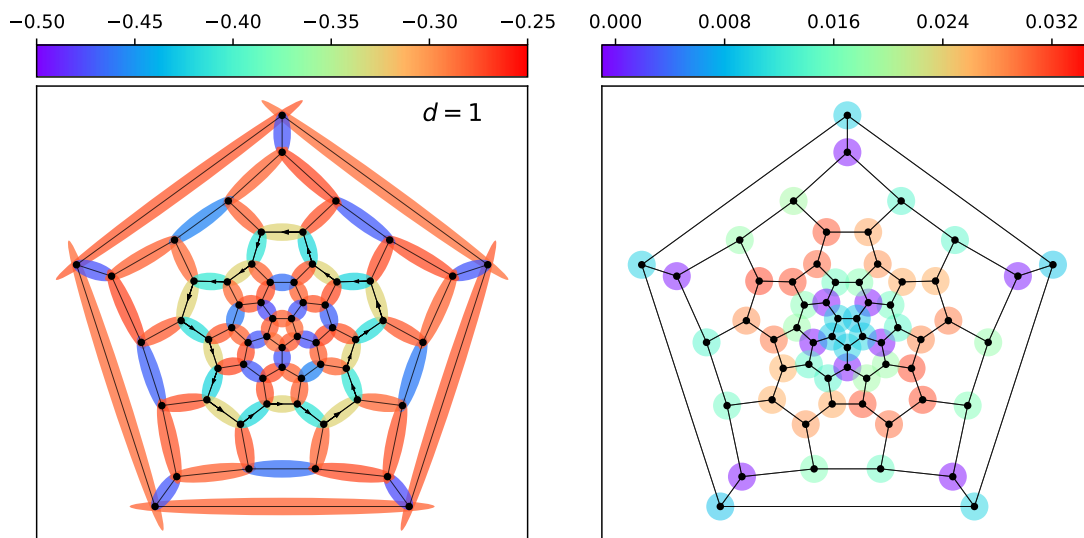
Figure 6: Left: Visualization of the nearest-neighbour spin-spin correlations $\langle \mathbf{S} \cdot \mathbf{S}_{d=1} \rangle$ in the lowest triplet state, $S_{\text{tot}} = 1$. The 20-site ring of altered correlations is highlighted with arrows. Right: Visualization of the local spin $\langle \mathbf{S}_i \rangle$ in the same state.

Looking at the spin-spin correlations in the $S_{\text{tot}} = 0$ excited state in Fig. 7, we note that the singlet excitation is also characterized by a 20-site ring with altered correlations, albeit differently positioned. Once again, this indicates degeneracy and we can compare to the small molecules. Starting from the ground state, the lowest singlets of the icosahedron and dodecahedron both transform as A_u, H_g, A_g [26]; and of the icosidodecahedron as A_g, A_u, T_{1u} [22]. The former two show 5-fold degenerate excited singlets, while the latter shows a nondegenerate one; and C_{60} is once again more similar to the smaller molecules.

4 Thermodynamics

4.1 Technical notes

We incorporate finite temperatures into the DMRG code using standard techniques [53]. By doubling the degrees of freedom, we go from a description using the wavefunction to a description using the density operator. This density operator is again purified into a state vector, but all operators act on the physical sites only, so that the additional "ancilla" sites are automatically traced over when taking expectation values using the state $\left| \beta \right\rangle = \exp\left(-\beta H/2\right) \left| \beta = 0 \right\rangle$. The entanglement entropy between the physical sites and the ancillas becomes equal to the thermal entropy. Finally, we can initiate the state at infinite temperature $\beta = 1/T = 0$ by taking the ground state of the entangler Hamiltonian

$$H_{\beta=0} = \sum_i \mathbf{S}_i \cdot \mathbf{S}_{a(i)}, \tag{3}$$

where $a(i)$ indicates the ancilla site attached to the physical site i.

We then apply a propagation in β using the TDVP (time-dependent variational principle) algorithm [54] with a step size of $d\beta = 0.1$. At each time step we have the choice of whether to
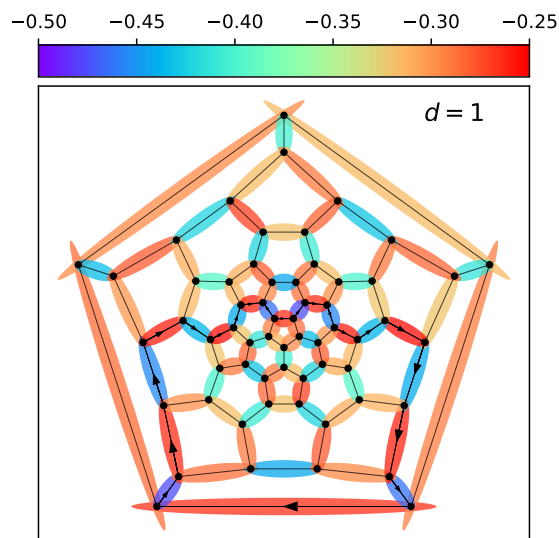
Figure 7: Visualization of the nearest-neighbour spin-spin correlations $\langle \mathbf{S} \cdot \mathbf{S}_{d=1} \rangle$ in the first excited singlet state, $S_{\text{tot}} = 0$. The 20-site ring of altered correlations in the lower part is highlighted with arrows.

apply the two-site algorithm which allows to dynamically grow the bond dimension from the initial product state; or the one-site algorithm which does not increase the bond dimension, but is much faster. Since an upper limit must be in any case set on the bond dimension in the calculations, it is no longer useful to use the two-site algorithm once it saturates. At this point we switch to the faster one-site algorithm (typically around $\beta = 6 - 10$). There is also the technical question of whether to incorporate the ancillas as separate sites (at the cost of longer-ranged hopping) or as "super-sites" [53]. We take the super-site approach for better accuracy.

The TDVP algorithm is known to get stuck in a product state without being able to build up the initial entanglement [21]. We find that this happens whenever the sites i and $i+1$ are not connected by a nearest-neighbour bond. Since we have chosen super-sites and a numbering where i and $i+1$ are always connected (see Sec. 2.1), this problem does not appear in our computations.

To strike a balance between accuracy and running time, we can limit the bond dimension *per subspace* to $\chi_{\text{sub,SU(2)}} \sim 300 - 600$, rather than limiting the total bond dimension. This ensures that the largest matrix is at most $\chi_{\text{sub,SU(2)}} \times \chi_{\text{sub,SU(2)}}$ and the duration of the remaining propagation can be estimated. The downside is that the resulting $\chi_{\text{SU(2)}}$ at each site does not in general correspond to the $\chi_{\text{SU(2)}}$ lowest singular values and has to be seen as an order-of-magnitude estimate. A benchmark of this approach for the numerically solvable C_{20} is given in Appendix A. Table 3 shows the parameters that were used in the thermodynamic calculations.

The relevant quantities are the partition function

$$Z_\beta = \langle \beta | \beta \rangle, \tag{4}$$

the internal energy

$$E(\beta) = \langle H \rangle_\beta = Z_\beta^{-1} \langle \beta | H | \beta \rangle, \tag{5}$$

the specific heat per site (or per spin):

$$c(T) = \frac{C(T)}{L} = \frac{1}{L} \frac{\partial E}{\partial T} = \frac{1}{L} \beta^2 \left[\langle H^2 \rangle_\beta - \langle H \rangle_\beta^2 \right], \tag{6}$$

Table 3: Parameters of the thermodynamic calculations. For an explanation of the bond dimensions, see Tab. 1. The underlined values were fixed.

$\chi_{\text{sub,SU(2)}}$	$\chi_{\text{SU(2)}}$	χ_{eff}
<u>300</u>	~ 2000	~ 16000
<u>400</u>	~ 3000	~ 20000
<u>600</u>	~ 4700	~ 36700
1163	<u>3000</u>	~ 13600
1507	<u>4000</u>	~ 17500

and the zero-field uniform magnetic susceptibility

$$\chi = \frac{1}{L} \lim_{\mathbf{B} \to 0} \nabla_{\mathbf{B}} \cdot \mathbf{M} = \frac{1}{L} \beta \big[\left\langle \mathbf{S}^2 \right\rangle_\beta - \left\langle \mathbf{S} \right\rangle_\beta^2 \big], \tag{7}$$

where $\mathbf{M}$ is the magnetization at a given external field strength $\mathbf{B}$ and the Hamiltonian is changed to $H \to H - \mathbf{B} \cdot \mathbf{S}$, with the total spin $\mathbf{S}$:

$$\mathbf{M} = \left\langle \mathbf{S} \right\rangle_{\mathbf{B},\beta} = Z_{\mathbf{B},\beta}^{-1} \left\langle \beta = 0 \middle| \mathbf{S} \, e^{-\beta(H - \mathbf{B} \cdot \mathbf{S})} \middle| \beta = 0 \right\rangle. \tag{8}$$

While the specific heat could be exactly calculated using the squared Hamiltonian average $\left\langle H^2 \right\rangle_\beta$, in practice this becomes quite expensive at every β-step, so we use a numerical differentiation of $E(\beta)$ with spline interpolation instead.

4.2 Specific heat

The result for $c(T)$ is shown in Fig. 8 and is compared to smaller molecules that exhibit a two-peak structure: For the truncated tetrahedron they are so close to each other that they cannot be resolved, while being distinct for the dodecahedron. For C_{60}, we find instead a high-T peak (around $T \sim 0.58$) and low-T shoulder (around $T \sim 0.15 - 0.19$). The high-T peak can be attributed to the energy scale given by $J = 1$ and is a general feature of Heisenberg chains [53, 55, 56]. The low-T peak can be attributed to the second scale of the energy gap. This can also be compared to the specific heat of the icosidodecahedron, which has three peaks [28, 30, 31]. The middle peak points to the presence of another gap in the region of low-energy states which is absent in the other systems.

We recall that for a two-level system given by the Hamiltonian $H = \text{diag}(0, \Delta)$, the specific heat has a Schottky peak at $T/\Delta \approx 0.417$. In other words, a maximum appears when the temperature is tuned to the middle of the gap Δ. This is roughly consistent with the gap values given in Tab. 1. The fact that we have a shoulder rather than a clear peak implies that several states of close energy contribute to $c(T)$, i.e. a comparatively high density of states close to the first excited state. In fact, we can see that as the bond dimension in the DMRG calculation is increased, we are able to better describe the low-lying states, leading to a flattening of a very shallow peak to a shoulder. Furthermore, we can say that the states in this vicinity must be singlets or triplets, since the quintet gap lies even higher (see Tab. 1).

The icosidodecahedron has been called "kagomé on a sphere" [27], since both geometries have corner-sharing triangles, and several attempts have been made to relate the two systems to each other [30, 31]. The low-energy properties of the kagomé lattice are not entirely clear, however: Some results point to a gapped state with a singlet-triplet gap of 0.13 and a very small neutral gap of ~ 0.05 [18, 19, 57], others to a gapless phase [58–62]. In the case of a molecule, a fair comparison should in any case be to a finite kagomé plaquette that has a finite-size gap.
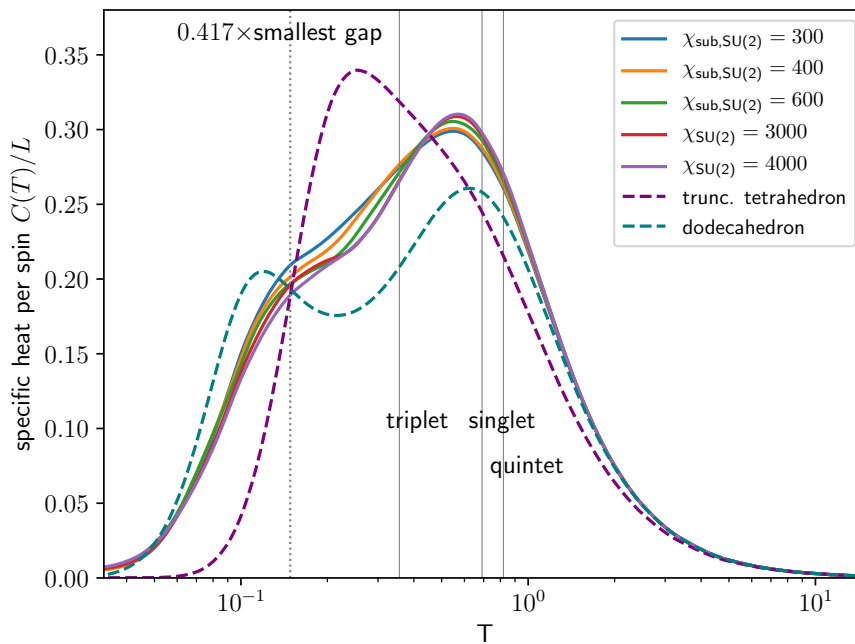
Figure 8: Specific heat of C_{60} for different bond dimensions (Eq. 6). The grey vertical lines indicate the triplet, singlet and quintet gaps with respect to the ground state. The dotted vertical line indicates 0.417 times the lowest gap (triplet). For the parameters, compare Tab. 3.

The low-temperature behaviour of the specific heat is consequently also very difficult to establish. What is well-established is the position of the main peak at $T \approx 0.67$ [16, 63, 64] and a shoulder below it at $T \sim 0.1 - 0.2$. At a very small $T \sim 0.01$ another peak is found in a finite system which moves up to merge with the shoulder as the system size is increased [64], while tensor-network calculations directly in the thermodynamic limit show no such peak in the first place [63]. The shoulder below the main peak is remarkably similar to the shape that we obtain for C_{60}. We also note that the main peak lies below $T = 1$ for both C_{60} and the kagomé lattice, while it is above $T = 1$ for the icosidodecahedron [28]. Since the specific heat is a function of eigenvalues only, we may wonder if the geometry of six triangles around a hexagon of the kagomé lattice leads to a similar eigenvalue distribution as for C_{60} (which has three pentagons around each hexagon) for singlet and triplet excitations that contribute around $T \sim 0.1 - 0.2$. On the other hand, the large number of singlets close to the kagomé ground state [65] is clearly better matched by the strongly frustrated icosidodecahedron.

4.3 Spin susceptibilty

Figure 9 shows the result for the susceptibility $\chi(T)$. It can be interpreted in a similar way, the difference being that singlet states do not contribute anymore. Moreover, it is easy to show that for high temperatures, $\chi(T)$ follows a universal Curie law $\chi(T) \sim 3/4 \cdot T^{-1}$, while for $T \to 0$ we expect $\chi \to 0$, since the ground state is a spin singlet and not susceptible to small fields. In between, $\chi(T)$ should have at least one peak. We observe that it is positioned at a higher temperature for the truncated tetrahedron due to the larger singlet-triplet gap (see Tab. 2). The dodecahedron and C_{60}, on the other hand, are remarkably close, though $\chi(T)$ tends to be slightly larger for C_{60} and does not go to zero as fast for very small temperatures, which we ascribe to the smaller singlet-triplet gap.
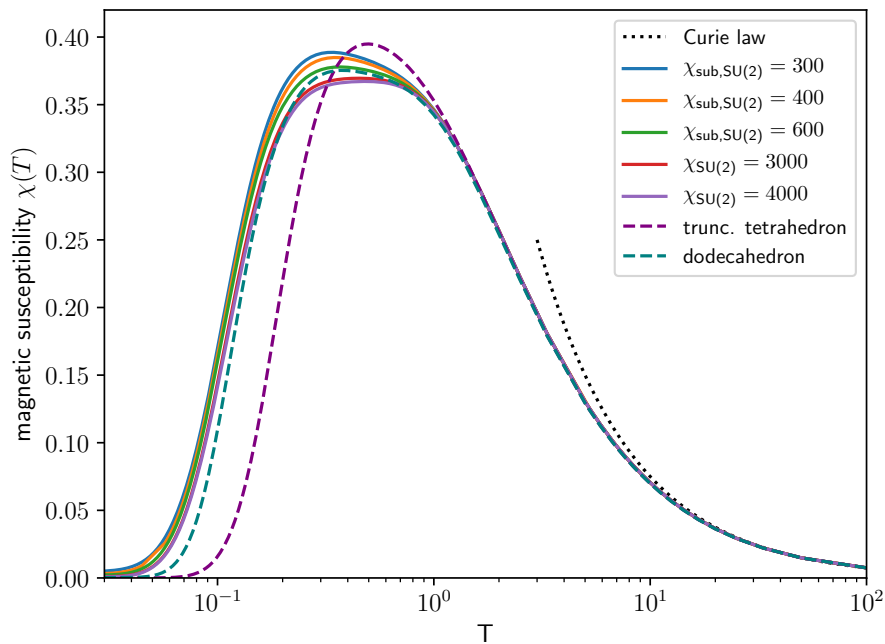
Figure 9: Zero-field uniform magnetic susceptibility C_{60} (Eq. 7) for different bond dimensions. Parameters as in Fig. 8.

5 Conclusion

We have presented a solution of the Heisenberg model on the C_{60} fullerene geometry. The spin-spin correlations in the ground state can be determined very accurately using DMRG and indicate that the C_{60} molecule is large enough not to be fully correlated across its full extent. The strongest correlations are found along an alternating path of hexagon and pentagon bonds, a consequence of the fact that the hexagons are not frustrated. Furthermore, for large distances, we find a deviation from the staggered sign pattern of an antiferromagnet.

Most strikingly (and unlike smaller fullerenes), the first excited state is a triplet and not a singlet, indicating weaker frustration. This can be attributed to the large number of unfrustrated hexagon faces, suggesting that frustration is tuneable in small fullerenes as a function of their size. Still, we find that the ground state of C_{60} is disordered with a very short correlation length of $\xi \approx 1.2 \sim 1.4$.

Thus, taking the point of view of the pentagons we can say that the frustration is significantly lowered because all the pentagonal faces are separated from each other by hexagons. On the other hand, taking the point of view of the hexagons we can say that a Néel-like state is prevented by the perturbing pentagonal faces, and one would need larger fullerenes to approach the honeycomb lattice limit.

In terms of thermodynamics, we find a two-peak structure of the specific heat, similar to what is found for the dodecahedron or the kagomé lattice down to $T \sim 0.1 - 0.2$. The low-temperature feature is very shallow for C_{60}, forming a shoulder, which indicates relatively densely lying singlet and triplet excited states. The spin susceptibility shows a broad peak very similar to the dodecahedron, but approaches zero less rapidly for $T \rightarrow 0$.

All the properties of C_{60} are quite different from the icosidodecahedron, which is highly frustrated, with many low-energy singlet states, a non-degenerate first excited singlet and

triplet, as well as a three-peak structure in the specific heat. On the other hand, we observe much similarity to the truncated tetrahedron: Most notably, the lowest excited state is a triplet and the spin-spin correlations follow the same pattern of being stronger for the same-face hexagon and acquiring a mixed sign for large distances.

We have not attempted to find out the spatial symmetry transformations of the lowest eigenstates, but can conclude that the ground state is non-degenerate, while the first excited singlet and triplet are degenerate, based on the breaking of spatial symmetries or its absence. Another open question is whether the frustrated pentagons can still measurably affect any properties of C_n in the large-n limit. DMRG is well equipped to answer these questions and solve the Heisenberg model for even larger n, or for fullerene dimers [66]. Another system that is well-suited for DMRG is the encapsulation of magnetic rare-earth atoms by fullerenes or fullerene-like molecules [67–69], inasfar these can be simulated by the Heisenberg model.

We also attempted to solve the full Hubbard model on the C_{60} geometry, but find that the variance per site is several orders of magnitude higher, so that one would also require an even higher bond dimension at a higher numerical complexity of twice the local Hilbert space size, while probably still tolerating larger errors. An improvement that can bring us closer to the Hubbard case at half filling could in principle be achieved by including higher orders in $1/U$. Up to $\mathcal{O}\left(U^{-3}\right)$, we have $J = 4t^2/U - 16t^4/U^3$ and a next-nearest-neighbour term $J' = 4t^4/U^3$ [70–72] which may again increase frustration. At $\mathcal{O}\left(U^{-5}\right)$ a biquadratic term is induced whose inclusion would be quite difficult.

Another intriguing question is how the properties of the undoped C_{60} are related to the results of Jiang and Kivelson [8] that show an attractive pair binding in the doped system. Such pair binding is also present for the truncated tetrahedron [37,73], is weak for the cube [37], but absent for the dodecahedron [73]. This means that one has to study excitations that result from removing electrons within the t-J model, rather than flipping spins. One can hope to relate the attractive pair binding to a geometrical feature like the weak frustration (which C_{60} and the truncated tetrahedron have in common) and perhaps establish a picture that is analogous to the famous relation between resonating valence bond states and superconductivity [74].

Acknowledgements

A   Specific heat of C_{20}

As a benchmark of the thermal DMRG algorithm, we calculate the specific heat of the dodecahedron and show the results in Fig. 10. While the ground state offers no challenge for DMRG and converges in a matter of seconds, the β-propagation is more demanding and we see that a high bond dimension is required to get the precise location and height of the low-temperature peak. However, even smaller bond dimensions are able to qualitatively capture the general two-peak structure. The implication for C_{60} is that while we cannot claim that the
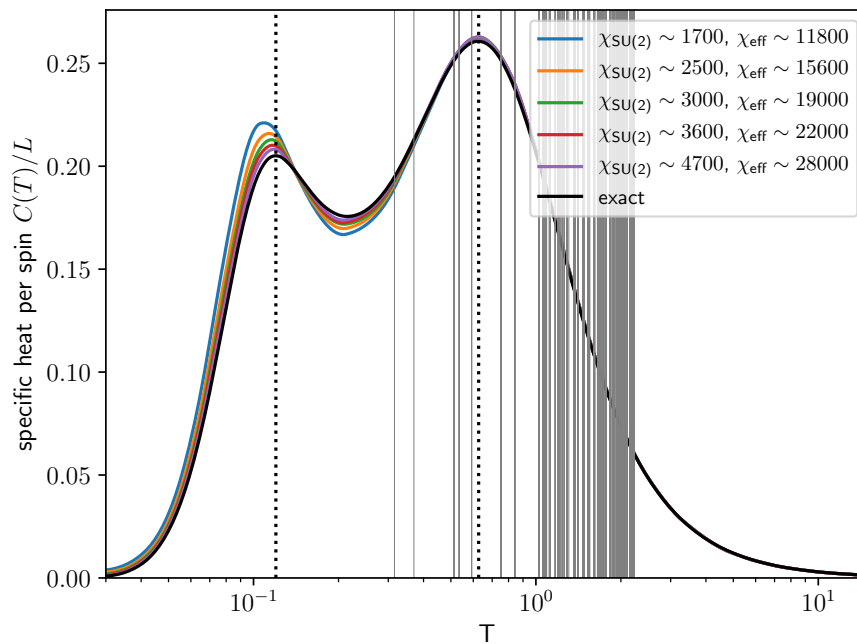
Figure 10: Specific heat of the dodecahedron for different bond dimensions. The bond dimension per subspace was limited to $\chi_{\mathrm{sub,SU(2)}} = 300, 400, 500, 600, 800$. The grey vertical lines indicate the first 1000 eigenenergies relative to the ground state, $E_n - E_0$. The dotted vertical lines indicate the peak positions from Ref. [26]. To obtain the exact result, we used the Kernel Polynomial Method [75] with 1000 lowest eigenstates, 1000 Chebyshev moments and 1000 random vectors.

finite-temperature results are numerically exact, since a much higher bond dimension may be required to achieve such precision, we expect that the qualitative behaviour should be captured as well.

References

[1] A. J. Stace and P. O'Brien, *Fullerenes: past, present and future, celebrating the 30th anniversary of Buckminster Fullerene*, Phil. Trans. R. Soc. A. **374**, 20160278 (2016), doi:10.1098/rsta.2016.0278.

[2] S. C. Benjamin et al., *Towards a fullerene-based quantum computer*, J. Phys.: Condens. Matter **18**, S867 (2006), doi:10.1088/0953-8984/18/21/s12.

[3] C. B. Winkelmann, N. Roch, W. Wernsdorfer, V. Bouchiat and F. Balestro, *Superconductivity in a single-C_{60} transistor*, Nat. Phys. **5**, 876 (2009), doi:10.1038/nphys1433.

[4] A. F. Hebard, M. J. Rosseinsky, R. C. Haddon, D. W. Murphy, S. H. Glarum, T. T. M. Palstra, A. P. Ramirez and A. R. Kortan, *Superconductivity at 18 K in potassium-doped C_{60}*, Nature **350**, 600 (1991), doi:10.1038/350600a0.

[5] T. T. M. Palstra, O. Zhou, Y. Iwasa, P. E. Sulewski, R. M. Fleming and B. R. Zegarski, *Superconductivity at 40K in cesium doped C_{60}*, Solid State Commun. **93**, 327 (1995), doi:10.1016/0038-1098(94)00787-X.

[6] Y. Takabayashi and K. Prassides, *Unconventional high-T_c superconductivity in fullerides*, Phil. Trans. R. Soc. A. **374**, 20150320 (2016), doi:10.1098/rsta.2015.0320.

[7] M. Kim, Y. Nomura, M. Ferrero, P. Seth, O. Parcollet and A. Georges, *Enhancing superconductivity in A_3C_{60} fullerides*, Phys. Rev. B **94**, 155152 (2016), doi:10.1103/PhysRevB.94.155152.

[8] H.-C. Jiang and S. Kivelson, *Electronic pair binding and Hund's rule violations in doped C_{60}*, Phys. Rev. B **93**, 165406 (2016), doi:10.1103/PhysRevB.93.165406.

[9] F. Lin, E. S. Sørensen, C. Kallin and A. J. Berlinsky, *Strong correlation effects in the fullerene $C_2 0$ studied using a one-band Hubbard model*, Phys. Rev. B **76**, 033414 (2007), doi:10.1103/PhysRevB.76.033414.

[10] S. Chakravarty, M. P. Gelfand and S. Kivelson, *Electronic correlation effects and superconductivity in doped fullerenes*, Science **254**, 970 (1991), doi:10.1126/science.254.5034.970.

[11] G. Stollhoff, *Anomalous electron-lattice coupling in C_{60}*, Phys. Rev. B **44**, 10998 (1991), doi:10.1103/PhysRevB.44.10998.

[12] D. Coffey and S. A. Trugman, *Magnetic properties of undoped C_{60}*, Phys. Rev. Lett. **69**, 176 (1992), doi:10.1103/PhysRevLett.69.176.

[13] L. Bergomi, J. P. Blaizot, Th. Jolicoeur and E. Dagotto, *Generalized spin-density-wave state of the Hubbard model for C_{12} and C_{60} clusters*, Phys. Rev. B **47**, 5539 (1993), doi:10.1103/PhysRevB.47.5539.

[14] P. Sindzingre, G. Misguich, C. Lhuillier, B. Bernu, L. Pierre, Ch. Waldtmann and H.-U. Everts, *Magnetothermodynamics of the spin-$\frac{1}{2}$ Kagomé antiferromagnet*, Phys. Rev. Lett. **84**, 2953 (2000), doi:10.1103/PhysRevLett.84.2953.

[15] G. Misguich and B. Bernu, *Specific heat of the $S = \frac{1}{2}$ Heisenberg model on the kagome lattice: High-temperature series expansion analysis*, Phys. Rev. B **71**, 014417 (2005), doi:10.1103/PhysRevB.71.014417.

[16] G. Misguich and P. Sindzingre, *Magnetic susceptibility and specific heat of the spin-$\frac{1}{2}$ Heisenberg model on the kagome lattice and experimental data on $ZnCu_3(OH)_6Cl_2$*, Eur. Phys. J. B **59**, 305 (2007), doi:10.1140/epjb/e2007-00301-6.

[17] H. C. Jiang, Z. Y. Weng and D. N. Sheng, *Density matrix renormalization group numerical study of the kagome antiferromagnet*, Phys. Rev. Lett. **101**, 117203 (2008), doi:10.1103/PhysRevLett.101.117203.

[18] S. Yan, D. A. Huse and S. R. White, *Spin-liquid ground state of the $S = 1/2$ Kagome Heisenberg antiferromagnet*, Science **332**, 1173 (2011), doi:10.1126/science.1201080.

[19] S. Depenbrock, I. P. McCulloch and U. Schollwöck, *Nature of the spin-liquid ground state of the $S = 1/2$ Heisenberg model on the Kagome lattice*, Phys. Rev. Lett. **109**, 067201 (2012), doi:10.1103/PhysRevLett.109.067201.

[20] J.-W. Mei, J.-Y. Chen, H. He and X.-G. Wen, *Gapped spin liquid with Z_2 topological order for the kagome Heisenberg model*, Phys. Rev. B **95**, 235107 (2017), doi:10.1103/PhysRevB.95.235107.

[21] R. Schäfer, I. Hagymási, R. Moessner and D. J. Luitz, *Pyrochlore $s = \frac{1}{2}$ Heisenberg antiferromagnet at finite temperature*, Phys. Rev. B **102**, 054408 (2020), doi:10.1103/PhysRevB.102.054408.

[22] I. Rousochatzakis, A. M. Läuchli and R. Moessner, *Quantum magnetism on the Cairo pentagonal lattice*, Phys. Rev. B **85**, 104415 (2012), doi:10.1103/PhysRevB.85.104415.

[23] R. T. Scalettar, A. Moreo, E. Dagotto, L. Bergomi, T. Jolicoeur and H. Monien, *Ground-state properties of the Hubbard model on a C_{60} cluster*, Phys. Rev. B **47**, 12316 (1993), doi:10.1103/PhysRevB.47.12316.

[24] U. Schollwöck, *The density-matrix renormalization group in the age of matrix product states*, Ann. Phys. **326**, 96 (2011), doi:10.1016/j.aop.2010.09.012.

[25] H. Fripertinger, *The cycle index of the symmetry group of the fullerene C_{60}*, Match, Mulheim an der Ruhr, Germany **33**, 121 (1996).

[26] N. P. Konstantinidis, *Antiferromagnetic Heisenberg model on clusters with icosahedral symmetry*, Phys. Rev. B **72**, 064453 (2005), doi:10.1103/PhysRevB.72.064453.

[27] I. Rousochatzakis, A. M. Läuchli and F. Mila, *Highly frustrated magnetic clusters: The kagomé on a sphere*, Phys. Rev. B **77**, 094420 (2008), doi:10.1103/PhysRevB.77.094420.

[28] J. Schnack and O. Wendland, *Properties of highly frustrated magnetic molecules studied by the finite-temperature Lanczos method*, Eur. Phys. J. B **78**, 535 (2010), doi:10.1140/epjb/e2010-10713-8.

[29] J. Ummethum, J. Schnack and A. M. Läuchli, *Large-scale numerical investigations of the antiferromagnetic Heisenberg icosidodecahedron*, J. Magn. Magn. Mater. **327**, 103 (2013), doi:10.1016/j.jmmm.2012.09.037.

[30] N. Kunisada and Y. Fukumoto, *Theoretical study of spherical kagome clusters in $Mo_{72}V_{30}$ and $W_{72}V_{30}$*, Progr. Theor. Exp. Phys. 41I01 (2014), doi:10.1093/ptep/ptu036.

[31] N. Kunisada and Y. Fukumoto, *Dimer-dimer correlations and magnetothermodynamics of $S=1/2$ spherical kagome clusters in $W_{72}V_{30}$ and $Mo_{72}V_{30}$*, Phys. Proc. **75**, 687 (2015), doi:10.1016/j.phpro.2015.12.089.

[32] A. Müller, A. Maria Todea, J. van Slageren, M. Dressel, H. Bögge, M. Schmidtmann, M. Luban, L. Engelhardt and M. Rusu, *Triangular geometrical and magnetic motifs uniquely linked on a spherical capsule surface*, Angew. Chem. Int. Ed. **44**, 3857 (2005), doi:10.1002/anie.200500697.

[33] A. M. Todea et al., *Extending the $\{(Mo)Mo_5\}_{12}M_{30}$ capsule keplerate sequence: A Cr_{30} cluster of $S=3/2$ metal centers with a $Na(H_2O)_{12}$ encapsulate*, Angew. Chem. Int. Ed. **46**, 6106 (2007), doi:10.1002/anie.200700795.

[34] A. Müller et al., *Archimedean synthesis and magic numbers: "sizing" giant molybdenum-oxide-based molecular spheres of the Keplerate type*, Angew. Chem. Int. Ed. **38**, 3238 (1999), doi:10.1002/(SICI)1521-3773(19991102)38:21<3238::AID-ANIE3238>3.0.CO;2-6.

[35] N. P. Konstantinidis, *$s = \frac{1}{2}$ antiferromagnetic Heisenberg model on fullerene-type symmetry clusters*, Phys. Rev. B **80**, 134427 (2009), doi:10.1103/PhysRevB.80.134427.

[36] N. A. Modine and E. Kaxiras, *Variational Hilbert-space-truncation approach to quantum Heisenberg antiferromagnets on frustrated clusters*, Phys. Rev. B **53**, 2546 (1996), doi:10.1103/PhysRevB.53.2546.

[37] S. R. White, S. Chakravarty, M. P. Gelfand and S. A. Kivelson, *Pair binding in small Hubbard-model molecules*, Phys. Rev. B **45**, 5062 (1992), doi:10.1103/PhysRevB.45.5062.

[38] D. Coffey and S. A. Trugman, *Correlations for the S=1/2 antiferromagnet on a truncated tetrahedron*, Phys. Rev. B **46**, 12717 (1992), doi:10.1103/PhysRevB.46.12717.

[39] P. W. Fowler and D. Manolopoulos, *An Atlas of Fullerenes*, Courier Corporation Massachusetts, United States, ISBN 9780486453620 (2007).

[40] V. Elser and R. C. Haddon, *Icosahedral C_{60}: an aromatic molecule with a vanishingly small ring current magnetic susceptibility*, Nature **325**, 792 (1987), doi:10.1038/325792a0.

[41] I. P. McCulloch, *From density-matrix renormalization group to matrix product states*, J. Stat. Mech. P10014 (2007), doi:10.1088/1742-5468/2007/10/p10014.

[42] C. Hubig, I. P. McCulloch and U. Schollwöck, *Generic construction of efficient matrix product operators*, Phys. Rev. B **95**, 035129 (2017), doi:10.1103/PhysRevB.95.035129.

[43] E. Cuthill and J. McKee, *Reducing the bandwidth of sparse symmetric matrices*, In Proceedings of the 1969 24th National Conference, ACM '69, 157 (1969), doi:10.1145/800195.805928.

[44] M. Exler and J. Schnack, *Evaluation of the low-lying energy spectrum of magnetic Keplerate molecules using the density-matrix renormalization group technique*, Phys. Rev. B **67**, 094440 (2003), doi:10.1103/PhysRevB.67.094440.

[45] H. C. Jiang, Z. Y. Weng and T. Xiang, *Accurate determination of tensor network state of quantum lattice models in two dimensions*, Phys. Rev. Lett. **101**, 090603 (2008), doi:10.1103/PhysRevLett.101.090603.

[46] J. Sato, M. Shiroishi and M. Takahashi, *Correlation functions of the spin- antiferromagnetic Heisenberg chain: Exact calculation via the generating function*, Nucl. Phys. B **729**, 441 (2005), doi:10.1016/j.nuclphysb.2005.08.045.

[47] R. Ganesh, J. van den Brink and S. Nishimoto, *Deconfined criticality in the frustrated Heisenberg honeycomb antiferromagnet*, Phys. Rev. Lett. **110**, 127203 (2013), doi:10.1103/PhysRevLett.110.127203.

[48] S. L. Altmann and P. Herzig, *Point-group theory tables*, Oxford University Press, Oxford, United Kingdom, ISBN 9780198552260 (1994).

[49] V. Brouet, H. Alloul, S. Gàràj and L. Forrò, *NMR studies of insulating, metallic, and superconducting fullerides: Importance of correlations and Jahn–Teller distortions*, in Fullerene-Based Materials, Springer Berlin Heidelberg, ISBN 9783540201069 (2004), doi:10.1007/b94382.

[50] R. R. P. Singh and D. A. Huse, *Triplet and singlet excitations in the valence bond crystal phase of the kagome lattice Heisenberg model*, Phys. Rev. B **77**, 144415 (2008), doi:10.1103/PhysRevB.77.144415.

[51] A. M. Läuchli, J. Sudan and R. Moessner, $S = \frac{1}{2}$ *kagome Heisenberg antiferromagnet revisited*, Phys. Rev. B **100**, 155142 (2019), doi:10.1103/PhysRevB.100.155142.

[52] P. Prelovšek, K. Morita, T. Tohyama and J. Herbrych, *Vanishing Wilson ratio as the hallmark of quantum spin-liquid models*, Phys. Rev. Research **2**, 023024 (2020), doi:10.1103/PhysRevResearch.2.023024.

[53] A. E. Feiguin and S. R. White, *Finite-temperature density matrix renormalization using an enlarged Hilbert space*, Phys. Rev. B **72**, 220401 (2005), doi:10.1103/PhysRevB.72.220401.

[54] J. Haegeman, C. Lubich, I. Oseledets, B. Vandereycken and F. Verstraete, *Unifying time evolution and optimization with matrix product states*, Phys. Rev. B **94**, 165116 (2016), doi:10.1103/PhysRevB.94.165116.

[55] T. Xiang, *Thermodynamics of quantum Heisenberg spin chains*, Phys. Rev. B **58**, 9142 (1998), doi:10.1103/PhysRevB.58.9142.

[56] H.-J. Schmidt, A. Hauser, A. Lohmann and J. Richter, *Interpolation between low and high temperatures of the specific heat for spin systems*, Phys. Rev. E **95**, 042110 (2017), doi:10.1103/PhysRevE.95.042110.

[57] J.-W. Mei, J.-Y. Chen, H. He and X.-G. Wen, *Gapped spin liquid with $\mathbb{Z}_2$ topological order for the kagome Heisenberg model*, Phys. Rev. B **95**, 235107 (2017), doi:10.1103/PhysRevB.95.235107.

[58] H. Nakano and T. Sakai, *Numerical-diagonalization study of spin gap issue of the kagome lattice Heisenberg antiferromagnet*, J. Phys. Soc. Jpn. **80**, 053704 (2011), doi:10.1143/JPSJ.80.053704.

[59] Y. Iqbal, F. Becca, S. Sorella and D. Poilblanc, *Gapless spin-liquid phase in the kagome spin-$\frac{1}{2}$ Heisenberg antiferromagnet*, Phys. Rev. B **87**, 060405 (2013), doi:10.1103/PhysRevB.87.060405.

[60] H. J. Liao, Z. Y. Xie, J. Chen, Z. Y. Liu, H. D. Xie, R. Z. Huang, B. Normand and T. Xiang, *Gapless spin-liquid ground state in the $s = 1/2$ Kagome antiferromagnet*, Phys. Rev. Lett. **118**, 137202 (2017), doi:10.1103/PhysRevLett.118.137202.

[61] Y.-C. He, M. P. Zaletel, M. Oshikawa and F. Pollmann, *Signatures of Dirac cones in a DMRG study of the Kagome Heisenberg model*, Phys. Rev. X **7**, 031020 (2017), doi:10.1103/PhysRevX.7.031020.

[62] S. Jiang, P. Kim, J. H. Han and Y. Ran, *Competing spin liquid phases in the $S=\frac{1}{2}$ Heisenberg model on the Kagome lattice*, SciPost Phys. **7**, 006 (2019), doi:10.21468/SciPostPhys.7.1.006.

[63] X. Chen, S.-J. Ran, T. Liu, C. Peng, Y.-Z. Huang and G. Su, *Thermodynamics of spin-1/2 Kagomé Heisenberg antiferromagnet: algebraic paramagnetic liquid and finite-temperature phase diagram*, Sci. Bull. **63**, 1545 (2018), doi:10.1016/j.scib.2018.11.007.

[64] J. Schnack, J. Schulenburg and J. Richter, *Magnetism of the $N = 42$ kagome lattice antiferromagnet*, Phys. Rev. B **98**, 094423 (2018), doi:10.1103/PhysRevB.98.094423.

[65] C. Waldtmann, H.-U. Everts, B. Bernu, C. Lhuillier, P. Sindzingre, P. Lecheminant and L. Pierre, *First excitations of the spin 1/2 Heisenberg antiferromagnet on the kagomé lattice*, Eur. Phys. J. B **2**, 501 (1998), doi:10.1007/s100510050274.

[66] N. P. Konstantinidis, *Ground state magnetic response of two coupled dodecahedra*, J. Phys.: Condens. Matter **28**, 016001 (2015), doi:10.1088/0953-8984/28/1/016001.

[67] X. Lu, T. Akasaka and S. Nagase, *Rare earth metals trapped inside fullerenes - Endohedral Metallofullerenes (EMFs)*, in Rare Earth Coordination Chemistry, John Wiley & Sons, Ltd, Chichester, UK, ISBN 9780470824870 (2010), doi:10.1002/9780470824870.ch7.

[68] J. Wang, Y. Liu and Y.-C. Li, *Magnetic silicon fullerene*, Phys. Chem. Chem. Phys. **12**, 11428 (2010), doi:10.1039/B923865D.

[69] J. Zhao, X. Huang, P. Jin and Z. Chen, *Magnetic properties of atomic clusters and endohedral metallofullerenes*, Coord. Chem. Rev. **289-290**, 315 (2015), doi:10.1016/j.ccr.2014.12.013.

[70] L. N. Bulaevskiĭ, *Quasihomopolar electron levels in crystals and molecules*, Sov. J. Exp. Theor. Phys. **24**, 154 (1967).

[71] M. Takahashi, *Half-filled Hubbard model at low temperature*, J. Phys. C: Solid State Phys. **10**, 1289 (1977), doi:10.1088/0022-3719/10/8/031.

[72] D. J. Klein and W. A. Seitz, *Perturbation expansion of the linear Hubbard model*, Phys. Rev. B **8**, 2236 (1973), doi:10.1103/PhysRevB.8.2236.

[73] F. Lin, E. S. Sørensen, C. Kallin and A. John Berlinsky, *Extended Hubbard model on a C_{20} molecule*, J. Phys.: Condens. Matter **19**, 456206 (2007), doi:10.1088/0953-8984/19/45/456206.

[74] P. W. Anderson, G. Baskaran, Z. Zou and T. Hsu, *Resonating-valence-bond theory of phase transitions and superconductivity in La_2CuO_4-based compounds*, Phys. Rev. Lett. **58**, 2790 (1987), doi:10.1103/PhysRevLett.58.2790.

[75] A. Weiße, G. Wellein, A. Alvermann and H. Fehske, *The kernel polynomial method*, Rev. Mod. Phys. **78**, 275 (2006), doi:10.1103/RevModPhys.78.275.